


Integrated use of georadar, electrical resistivity, and SPT for site characterization and water content estimative

Érdeson Soares Farias¹ , Sandro Lemos Machado^{1#} , Heraldo Luiz Giacheti² ,
Alexsandro Guerra Cerqueira³ 

Case Study

Keywords

In situ tests
Site characterization
GPR
ERT
SPT
Coupled surveys

Abstract

Geophysical methods are potent tools for geotechnical site characterization in a non-destructive way. They improve the extrapolation of punctual data from direct survey methods, allowing a fast and cost-effective evaluation of large areas. Ground Penetrating Radar (GPR) and DC electrical resistivity (ER) are the most requested methods for geotechnical and geoenvironmental applications. Their use, however, is usually uncoupled, with no sharing of information from one method to another to improve data interpretation. This case study illustrates the development of protocols and scripts in R[®] programming language for ER and GPR data analysis with Standard Penetration Tests (SPT) data to produce more accurate information on subsurface conditions concerning lithology, water content, and groundwater table (GWT) position. The SPT data were used to associate resistivity ranges with different soil lithologies and GPR pulse velocities for estimating the soil water content. Estimated water content values aided in interpreting ER data and locating the groundwater table. The contacts between layers in the radargrams allowed the refinement of the ER model, rendering 3D volumes for each soil layer in situ.

1. Introduction

Geotechnical and geoenvironmental applications use the Ground Penetrating Radar (GPR) and electrical resistivity geophysical investigation methods intensively. They provide the possibility of extrapolating punctual geotechnical surveys, allowing a better and less expensive subsurface characterization (Cosenza et al., 2006). GPR is a non-destructive subsurface investigation method based on the propagation and reflection of electromagnetic pulses. It has proven to be a high-resolution, time and cost-efficient subsurface imaging method for geotechnical applications. GPR, however, presents limitations in the case of high-conductivity soils because of their elevated electrical conductivity, which causes GPR's signal attenuation. GPR's most common geotechnical applications are related to the subsurface location of buried structures such as pipes, galleries, and tanks and detection of different soil layer interfaces (Souza & Gandolfo, 2012). The reflections caused by an object crossing the radargram plane will form a hyperbola (Davis & Annan, 1989), a function of the velocity of propagation of the electromagnetic pulse (V), as illustrated in Equation 1:

$$V = \frac{2\sqrt{x^2 + z^2}}{t} \quad (1)$$

where x is the horizontal distance between the antenna's center and the object's center, z is its depth, and t is the two-way travel time. The value of V is a function of the electromagnetic properties of the propagation medium, and it can be estimated using an expression derived from Maxwell's equation (Equation 2):

$$V = \frac{C}{\sqrt{\frac{\mu\epsilon}{2} \left[\sqrt{1 + \left(\frac{\sigma}{\omega\epsilon}\right)^2} + 1 \right]}} \quad (2)$$

where C is the light propagation in vacuum (3.10^8 m/s), σ is the medium electrical conductivity (S/m), ω is the angular frequency (rad/s), μ ($\mu = 4\pi \times 10^{-7}$ T m/A in vacuum, μ_0) is the magnetic permeability, and ϵ is the electric permittivity ($\epsilon = 8.854$ C²/N m² in a vacuum, ϵ_0) (Topp & Davis, 1981; Topp et al., 1980). Most minerals and fluids present values of μ close to μ_0 . However, values of ϵ can vary widely in soils due to the soil water content. Furthermore, for the pulse

#Corresponding author. E-mail address: smachado@ufba.br

¹Universidade Federal da Bahia, Departamento de Ciência e Materiais, Salvador, BA, Brasil.

²Universidade Estadual Paulista "Júlio de Mesquita Filho", Escola de Engenharia, Bauru, SP, Brasil.

³Universidade Federal da Bahia, Departamento de Geofísica, Salvador, BA, Brasil.

Submitted on June 10, 2022; Final Acceptance on May 18, 2023; Discussion open until November 30, 2023.

<https://doi.org/10.28927/SR.2023.006422>



This is an Open Access article distributed under the terms of the Creative Commons Attribution License, which permits unrestricted use, distribution, and reproduction in any medium, provided the original work is properly cited.

frequencies used by GPR (0.02 to 2.5 GHz), the medium conductivity has a minor influence on the pulse propagation velocity, which can be approximated by Equation 3 (Davis & Annan, 1989):

$$V = \frac{C}{\sqrt{\varepsilon_r}} \quad (3)$$

where $\varepsilon_r = \varepsilon/\varepsilon_0$ is the relative dielectric constant of the medium.

Table 1 illustrates typical values of relative dielectric constant, electrical conductivity, and propagation velocity for different materials. As observed, water content significantly influences the pulse propagation velocity because of its high dielectric constant ($\varepsilon_r = 80$).

The interval velocity between two reflectors (V_{int}) can be calculated using Equation 4, proposed by Dix (1955), where V_n and V_{n-1} are the average velocities from the soil surface to the top of reflectors n and $n-1$ and, respectively, and t_n and t_{n-1} are the corresponding two-way travel times.

$$V_{int} = \sqrt{\frac{V_n^2 t_n - V_{n-1}^2 t_{n-1}}{t_n - t_{n-1}}} \quad (4)$$

Several studies related the soil water content with the propagation velocity of an electromagnetic pulse. The first contributions to this subject used the Time Domain Reflectometry (TDR) technique (Conciani et al., 1996; Topp & Davis, 1981; Topp et al., 1980). Similar concepts can be applied to GPR (Amparo et al., 2007; Botelho et al., 2003; Machado et al., 2006), although the position of the reflectors has yet to be discovered, contrary to TDR. Equation 5 was proposed (Botelho et al., 2003) based on the Wyllie equation for the elastic wave velocity of propagation (Wyllie et al., 1958) to estimate the gravimetric water content (w) in unsaturated soils. In this equation, ε_{rw} and ε_{rs} are the relative dielectric constants for water and soil solid particles, e is the soil void ratio, and G is the solid particles' relative density. According to the authors, for practical purposes, values of $\varepsilon_{rw} = 80$ and $\varepsilon_{rs} = 4.2$ (the relative dielectric constant for quartz) can be assumed for most cases.

$$w = \frac{\frac{C(e+1)}{V_{int}} - \sqrt{\varepsilon_{rs}} - e}{G(\sqrt{\varepsilon_{rw}} - 1)} \quad (5)$$

Grain size distribution, mineralogy, porosity, and water content/salinity are the main parameters controlling the soil's electrical resistivity (ρ). Furthermore, the soil cation exchange capacity (CEC) can indicate the mobility of the ions around soil particles. These ions facilitate the electrical current flow through the soil. Soil clay content and the predominance of 2:1 minerals such as bentonite and montmorillonite increase CEC (Nguyen, 2014). Thus, coarser soils present higher resistivity than silty and clayey soils. Electrical resistivity tomography (ERT) provides continuous 2D images of the subsoil, making it possible to analyze the ρ variations laterally and with depth (Souza & Gandolfo, 2012). The analysis of the resistivity sections allows for identifying the resistivity anomalies due to different lithologies and water contents or contaminant plumes in the subsurface (Sass et al., 2008).

Although demanding the injection of higher current intensities due to its low signal to noise ratio, the dipole-dipole arrangement allows rapid data acquisition and enables studying the lateral resistivity variations at different depths. In such an arrangement, the current (AB) and the potential (MN) dipoles are placed/aligned on the ground surface. The distance between the electrodes is kept constant and equal to a . The data acquisition starts with a minimum distance $x = 1 a$ between the pairs AB, and MN and the following measurements are performed by displacing the pairs of electrodes at multiples of a (Souza & Gandolfo, 2012). Although providing continuous 2D and even 3D images of the subsoil, ERT resolution is a function of the distance a , and its use for high-resolution images is time-consuming. According to Zorzi & Rigoti (2011), the depth investigation can vary from AN/4 to AN/10. Furthermore, soil resistivity is a function of its water content, varying along the year according to the dry/rainy seasons. Using ERT associated with GPR offers a possibility to overcome these drawbacks.

In recent years, there has been an increase in the simultaneous use of GPR and ERT in site investigations,

Table 1. Typical values of ε_r , σ and V for different materials (Davis & Annan, 1989).

Material	ε_r (-)	σ (mS/m)	V (m/ns)
Air	1	0	0.300
Water	80	0.01	0.033
Dry sand	3-5	0.01	0.150
Saturated sand	20-30	0.1-1	0.060
Limestone	4-8	0.5-2	0.120
Shale	5-15	1-100	0.090
Silt	5-30	1-100	0.070
Clay	5-40	2-100	0.060
Granite	4-60	0.01-1	0.130

although such use has been limited to geotechnical applications. The purpose of site investigations varies depending on its objective, ranging from soil characterization and layer interface delimitation (Evangelista et al., 2017); to geological studies in unsaturated karst zones (Carrière et al., 2013), assessment of the thickness of talus layers in the European Alps (Sass et al., 2008), and stratigraphical characterization of Quaternary sediments layers (Pellicer & Gibson, 2011). In such works, GPR data is used to better define the interface between layers or as an additional tool in delineating high attenuation (or high conductivity) zones detected by ERT surveys. The use of GPR data to estimate moisture content and assist in interpreting ERT data is scarce. No publications with such characteristics were found in the literature by the authors. This case study uses SPT, GPR, and ERT for site characterization, including the water content estimation and definition of groundwater table position. SPT and GPR data are used to improve the ERT 2D sections, and the results of the modified ERT sections are used to construct a 3D stratigraphical model.

2. Study site

The study site is located at the countryside (thorp of Água Branca, $12^{\circ}35'39.8''\text{S}$; $38^{\circ}26'06.2''\text{W}$) of the city of São Sebastião do Passé, Bahia, Brazil, about 68 km from the capital of Bahia. The local geology is dominated by the Todos os Santos sedimentary Bay, formed from the evolution of the crustal stretching, which caused the fragmentation of the Gondwana supercontinent in the Mesozoic era (Lima, 1999).

Sediments of the São Sebastião and Barreira Formations and Quaternary deposits predominate in the study area (Figure 1). The São Sebastião Formation is a fluvial deposit lithologically composed of fine to coarse sandstones interspersed with silty clay layers. The typical composition of the clayey

layers presents kaolinite and illite with a considerable amount of iron oxides (Souza et al., 2004).

Due to its high effective porosity and hydraulic conductivity, this formation is one of the most important underground water reserves of Todos os Santos Bay (Alves, 2015; Lima, 1999). The Barreira Formation is formed by fine sand and kaolinitic silty clay fractions with crossbedding and plane-parallel lamination. Its thickness ranges from 30 m to 40 m (Ghignone, 1979). The alluvial Quaternary sediments occur in shallower depths in valleys, floodplains, and the coast (Barbosa & Dominguez, 1996). Lithologically, they are poorly graded sandy sediments usually rich in organic matter. According to Lima (1999), the Reconcavo aquifer system, composed of the São Sebastião, Marizal, and Barreiras Formations, has a water reserve estimation of approximately five hundred billion cubic meters and is used to attend villages, cities, and industrial facilities.

3. In-situ site investigation campaign

The investigation campaign (Figure 2) used five SPTs boreholes excavated down to 15 m depth (ABNT, 2020), three ERT, and two GPR sections (Farias, 2021). Investigation line 3 was positioned close to SPT boreholes. SPT results (Figure 3) were used to interpret the ERT data and define the electrical resistivity ranges in the ERT sections. Unfortunately, the SPT performed tests could not detect groundwater table. The cisterns provided the only evidence concerning the groundwater table position in some residences' backyards during the rainy season.

ERT surveys used a Syscal Pro resistivity meter (Iris Instruments®) with ten channels and an internal transmitter with 250 W and 2000 V_{pp}, allowing the injection of a maximum current of 2.5 A into the soil. The integrated transmitter/receptor unities enable setting automatic reading scales

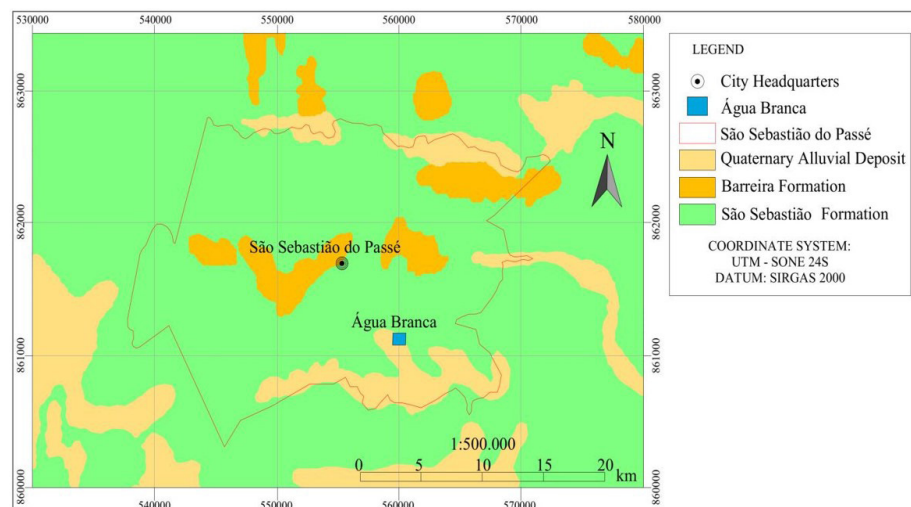


Figure 1. Lithology of the study site. Modified from Souza et al. (2004).



Figure 2. In situ tests carried out at the study site.

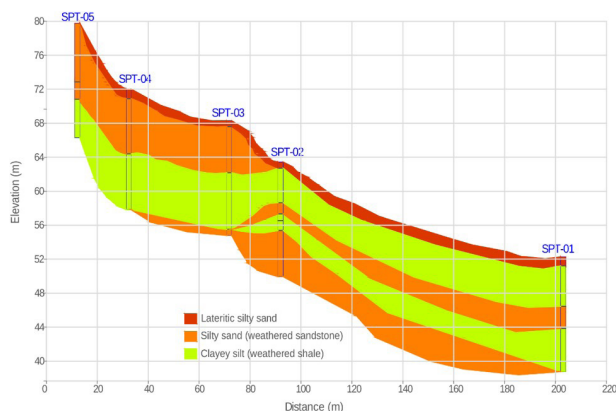


Figure 3. Associated soil profile obtained from SPT data. Adopted sobrelevation: 3.5.

and simultaneous measurements of apparent resistivity and chargeability. An inter-electrode spacing of $a = 10$ m was adopted (see Figure 4a). This value was adopted, aiming for a balance between ERT resolution and survey feasibility. The authors suggest a value of $a = 5$ m for better integration with GPR and SPT results for shallower investigations. A saline solution was used to improve the electrode/soil electrical conductivity. ERT surveys followed ABNT (2011).

The three ERT sections (ERT1, ERT2, and ERT3) had lengths of 270 m, 220 m, and 270 m, respectively. The experimental procedure initially positioned the two dipoles AB and MN in the first four electrodes and, while keeping the current dipole (AB) fixed, moving the potential dipole (MN) until a distance between the dipoles of $8a$. The procedure was then resumed by positioning the dipoles at electrodes 2 to 5 (offset from the last initial position of 1 a), and the procedure was repeated until the last possible position.

The ERT apparent resistivity was inverted using ZondRes2d[®] software. The inversion process adopted a maximum depth of 45 m and ten iterations. Based on the obtained results from ERT and SPT, the following correspondence between local lithology and electrical resistivity was assumed for the study area: Clayey silt (weathered shale): $\rho < 80 \Omega\text{m}$; Silty sand (weathered sandstone): $80 \Omega\text{m} \leq \rho < 180 \Omega\text{m}$ and Lateritic silty sand $\rho \geq 180 \Omega\text{m}$. Although shale layers, especially if saturated, usually present resistivity values less than $20 \Omega\text{m}$, in this case, the material is described as clayey silt with a considerable amount of fine sand. Similarly, the silty sand (weathered sandstone) layer has a significant amount of clay, which is likely responsible for its relatively low electrical resistivity values. The 2D ERT sections were georeferenced using a R[®] (2020) programming language script developed for this study, the local topography, and the location of the survey points. Similar procedures were adopted for GPR

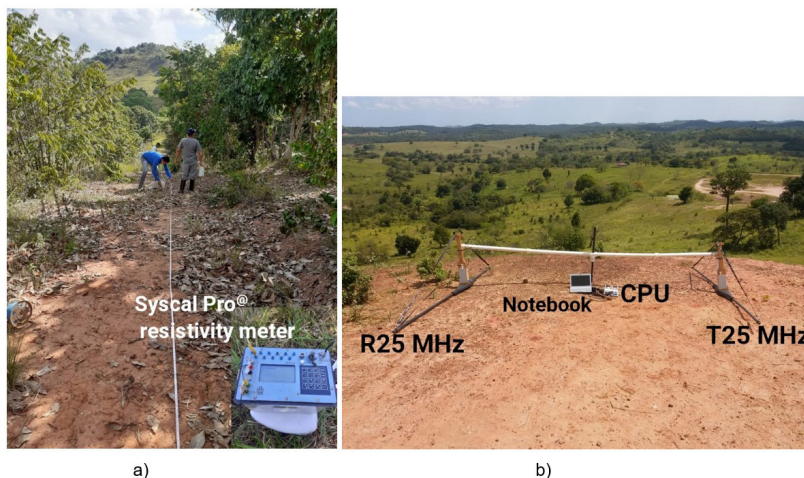


Figure 4. Field activities. a) ERT and b) GPR.

data, in this case, using a different script. The GPR surveys used Mala Geoscience[®] equipment consisting of central unit (CUII), odometer, 25 MHz antennas, and laptop (see Figure 4b). A constant offset of 4 m between the antennas and a step distance of 0.5 m were adopted. The time window was 800 ns, corresponding to an investigation depth of about 40 m, if a $V = 10$ cm/ns is initially assumed for the soil. These values follow those usually suggested in the technical literature (Davis & Annan, 1989). The GPR data were processed using a R[®] (2020) script and the RGPR Libraries (Huber & Hans, 2018) with the following filter sequence: time zero correction -> dewow -> bandpass filter -> power time. The obtained radargrams were analyzed, and the existent reflection hyperbolas were fitted using Equation 1. This procedure enabled the creation of a velocity field for each radargram, which was used to convert travel time to depth (or elevation). Radargrams were then geo-referenced using the developed scripts.

The R[®] (2020) scripts developed for this study allows GPR and ERT data to be superimposed for better comparison and the 3D interpolation of the field data. The interpolated data can be used to construct 3D interactive images to visualize the investigation campaign results better. Fitted hyperbolas were also used to calculate the interval velocities according to Equation 4 and then estimate soil water content (Equation 5). In this case, values of $G = 2.70$ and $e = 0.81$ were assumed based on the data from undisturbed samples.

4. Results and analysis

Figure 5 presents the resistivity contours for section ERT3 jointly with the lithology data from SPT. There is a fair agreement between interpolated resistivity and soil lithology. However, the distinction between the clayey silt (weathered shale) and silty sand (weathered sandstone) layers was only sometimes satisfactory. These discrepancies are influenced by groundwater table position (SPT and ERT were performed in different periods) and the similar texture of the layers, besides ERT resolution, around 5 m. Individual bore log details can be found in Farias (2021).

Figure 6a presents data from the GPR2 radargram after filtering. Figure 6b shows some adjusted hyperbola and possible layer interfaces. The radargrams' hyperboles are valuable information often neglected in GPR surveys. They allow underground water content estimations using the TDR principles as previously discussed. Furthermore, the indicated layer interfaces help separate the different soil layers, adding resolution to the ERT surveys. Depth (z) and mean pulse velocity (V) are also indicated in Figure 6b (Equation 1). Figure 6c highlights high attenuation zones and crossbedding, which are coherent with the layering pattern observed in some SPT samples and with the findings of Lima (1999) concerning the Barreira Formation. High attenuation zones (loss of GPR return signal) in radargrams indicate the presence of high plasticity soils, which absorb most of the electrical-magnetic pulse energy due to their high electrical conductivity.

The high attenuation zones shown in Figure 6c were used with the estimated soil water contents to indicate the occurrence of the saturated shale layer. Equation 5 provided w estimations from V_{int} , which were calculated using the values of V presented in Figure 6b (Equation 4). Higher values of V are observed on the left side of the radargram (Figure 6b), indicating less saturated soil for shallower depths in this region. Figure 7 presents soil water content contours for GPR2 and indicates the probable position of the groundwater table. The soil was considered saturated for pulse velocities $V_{int} \leq 6.0$ cm/ns, corresponding to $w > 25\%$. This value follows the average value of void ratio of the collected specimens in the field (Farias, 2021). A sharp transition in the w values is noted on the left side of Figure 7, probably related to the occurrence of the sandstone (higher hydraulic conductivity) layer on the top of the shale layer. Therefore, rainwater is expected to infiltrate through sandstone and accumulate in the layers' interface. The groundwater table position obtained from GPR's surveys was coherent with the field observations performed in some cisterns located in the area during the rainy season.

Figure 8a presents the overlapping of ERT2 and GPR2 data. There is a good agreement between the high

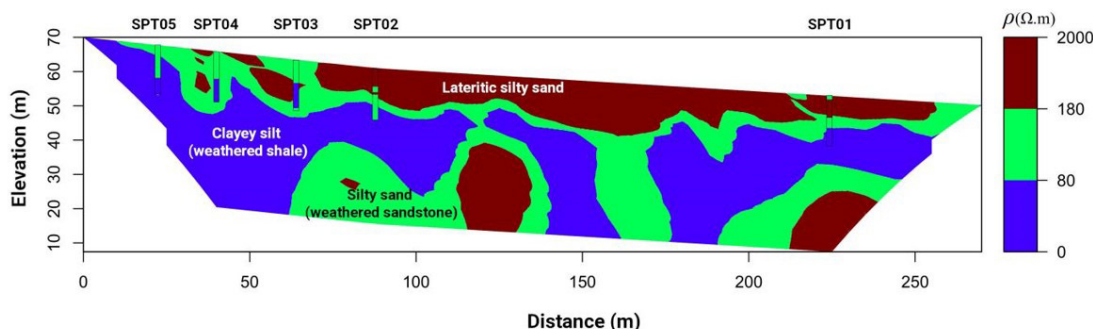


Figure 5. ERT3 inverted section and SPT.

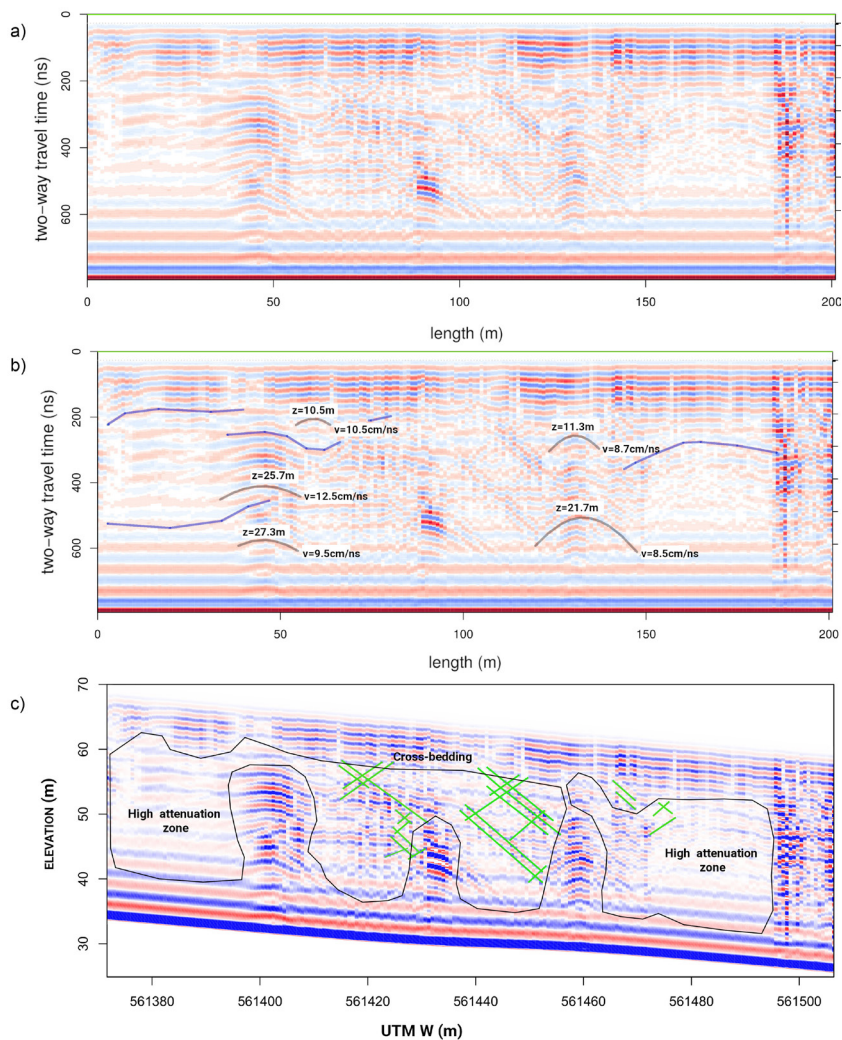


Figure 6. GPR2 radargram a) radargram after filtering sequence b) hyperbola fitting and c) crossbedding attenuation zones.

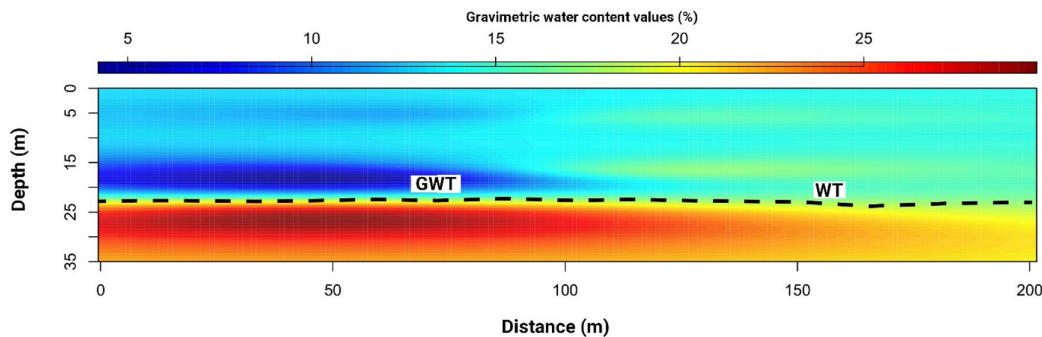
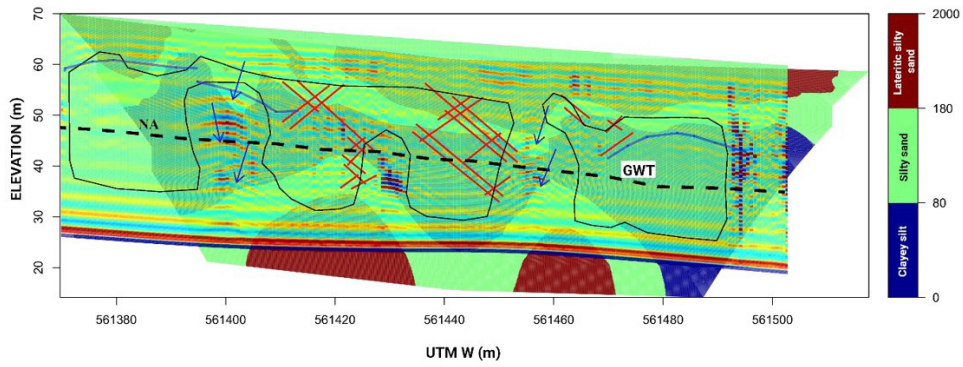


Figure 7. Contours of estimated water content values for GPR2 section.

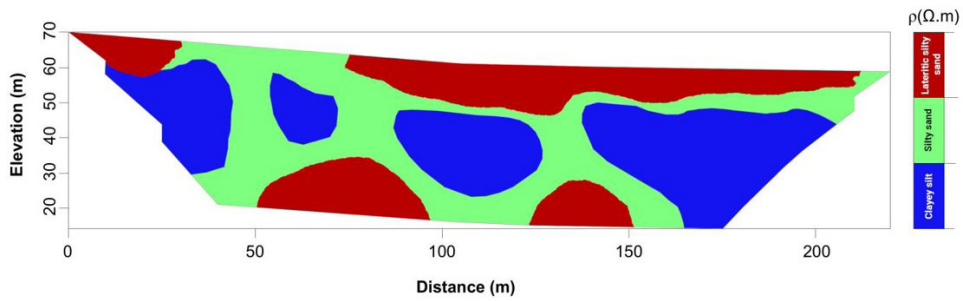
attenuation zones in GPR2 and the occurrence of the weathered shale layer indicated in ERT2.

The hyperbolas identified in the radargram appear to be related to the high-resistivity zones detected in the lower part of Figure 8a. Due to their position at great depths and below the water table, these data indicate that it is possible that it

is a different lithology than the shallower high-resistivity layer (silty lateritic sand). Figure 8b presents the modified ERT2 section after the coupled analysis of the SPTs, electrical resistivity, and GPR campaigns. Figure 9a presents the overlapping of ERT1 and GPR1 data. In this case, the high attenuation zones extend beyond the areas initially marked

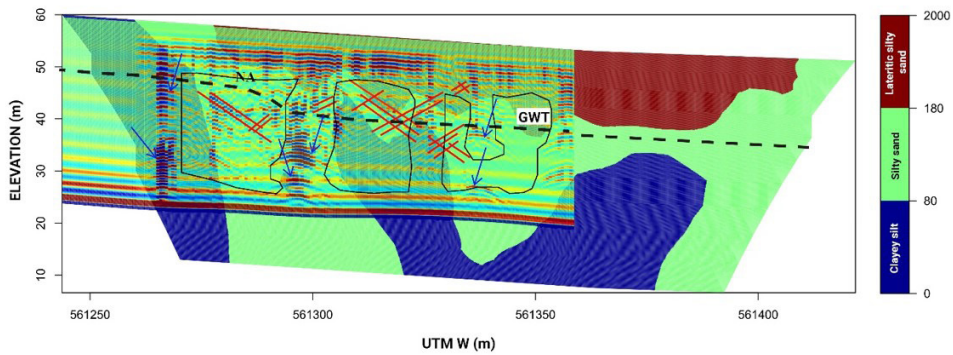


a)

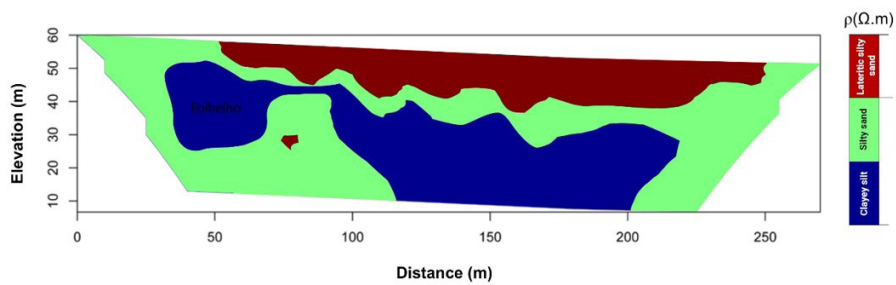


b)

Figure 8. a) ERT2 and GPR2 results overlapped and b) reinterpreted ERT2 section.



a)



b)

Figure 9. a) ERT1 and GPR1 results overlapped and b) reinterpreted ERT1 section.

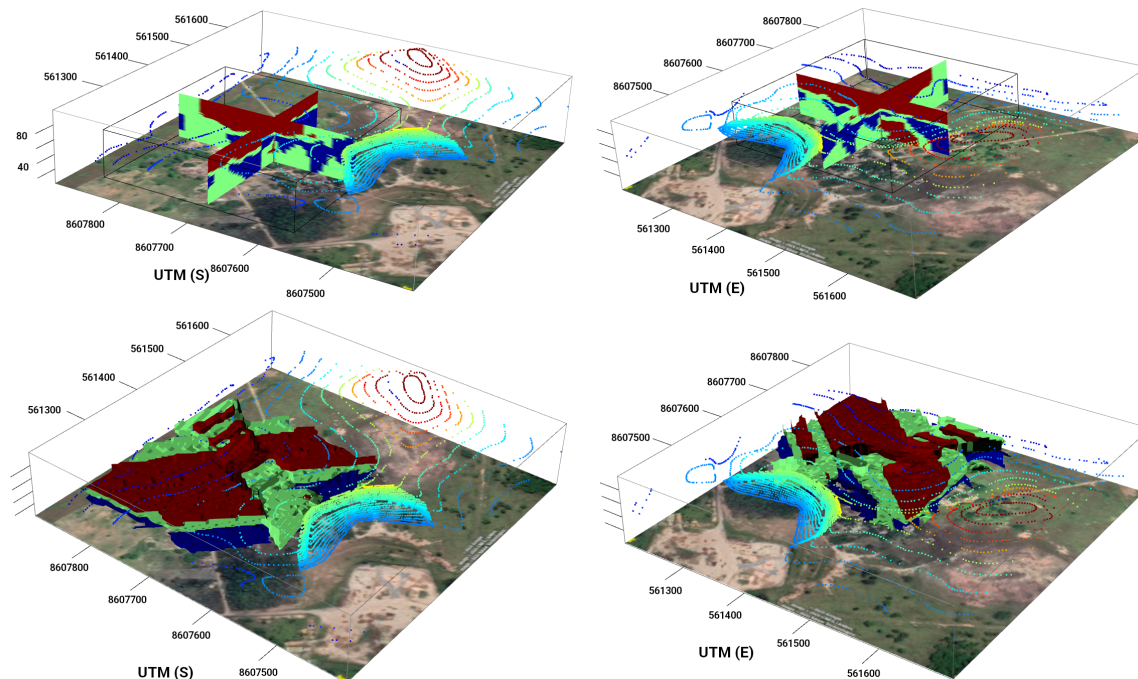


Figure 10. Typical sections of the elaborated 3D model.

as the weathered shale layer, motivating the changes in the ERT interpretation, as indicated in Figure 9b.

Figure 10 shows some sections of the 3D model obtained by interpolating the electrical resistivity values. Downloading the following links provide interactive versions of the Figure 10: Sections 3D (Machado, 2023a) and Surfaces 3D (Machado, 2023b).

5. Conclusion

Results from different direct and indirect investigation methods are presented and discussed to highlight how they can be used in a coupled manner for better characterization of subsurface conditions. The GPR data provided valuable information concerning the high conductance zones and aided in delimitating the contacts between the different layers in the field. In addition, the pulse propagation velocities obtained from hyperbola fitting were fundamental in correcting the radargram depth, also making it possible to estimate the soil moisture distribution and groundwater table location. The estimated moisture content values provided valuable information to interpret the ERT data since water can widely change ER values for a given soil formation. The SPT provided the basis for sketching the subsurface model, correlating the data from direct and indirect methods, and providing the information for ERT ranges definition. The developed activities in this case study may contribute to better site characterization, aggregating data from different sources, and analyzing the results in a coupled and interactive manner. The investigation procedures reduce doubts about

the geotechnical characteristics of the subsurface soil layers. Detection of the layer interface is improved, in addition to providing estimates of soil water content that helps define the groundwater table location.

Acknowledgements

The authors would like to thank the Research Center on Geophysics and Geology of the Federal University of Bahia who provided the electro resistivity meter used in the paper.

Declaration of interest

The authors have no conflicts of interest to declare. All co-authors have observed and affirmed the contents of the paper and there is no financial interest to report.

Authors' contributions

Érdeson Soares Farias: data curation, visualization, methodology, writing – original draft. Sandro Lemos Machado: methodology, supervision, writing – original draft. Heraldo Luiz Giacheti: writing – review and editing. Aleksandro Guerra Cerqueira: writing – review and editing.

Data availability

All data, models, or code that support the findings of this study are available from the corresponding author upon reasonable request.

List of symbols

a	distance between the electrodes
e	void ratio
t	two-way travel time
t_n	two-way travel time to reflector n
t_{n-1}	two-way travel time to reflector n-1
w	gravimetric humidity
x	horizontal distance between the antennas center to the center of the object
z	depth
$A, B, M,$ and N	letters assigned to electrodes in ER methods
C	velocity of propagation of light in a vacuum
CEC	cation exchange capacity
ER	electrical resistivity
ERT	electrical resistivity tomography
G	specific density
GWT	groundwater water table
GPR	ground penetrating radar
SPT	standard penetration test
TDR	time domain reflectometry
V	velocity of propagation of the electromagnetic pulse
V_n	average velocity from the soil surface to the top of reflector n
V_{n-1}	average velocity from the soil surface to the top of reflector n-1
V_{int}	interval velocity
ϵ	electric permittivity
ϵ_0	electric permittivity of vacuum
ϵ_r	relative dielectric constant
ϵ_{rs}	relative dielectric constant for soil solid particles
ϵ_{rw}	relative dielectric constant for water
μ	magnetic permeability
μ_0	magnetic permeability in vacuum
ρ	electrical resistivity
σ	electrical conductivity
ω	angular frequency

References

- ABNT NBR 15935. (2011). *Investigações ambientais — aplicação de métodos geofísicos*. ABNT - Associação Brasileira de Normas Técnicas, Rio de Janeiro, RJ (in Portuguese).
- ABNT NBR 6484. (2020). *Solo - sondagens de simples reconhecimento com SPT - método de ensaio*. ABNT - Associação Brasileira de Normas Técnicas, Rio de Janeiro, RJ (in Portuguese).
- Alves, J.E. (2015). *Estudos hidrogeoquímico comparativo entre os membros da Formação São Sebastião, Recôncavo Norte – BA* [Master's dissertation, Federal University of Bahia]. Federal University of Bahia repository (in Portuguese). Retrieved in May 18, 2023, from <https://repositorio.ufba.br/handle/ri/21557>
- Amparo, N.S., Machado, S.L., Botelho, M.A.B., & Dourado, T.C. (November 1-3, 2007). Uso de GPR como uma ferramenta não intrusiva para levantamento de perfis de umidade de campo. In Associação Brasileira de Mecânica dos Solos e Engenharia Geotécnica (Org.), *VI Simpósio Brasileiro de Solos Não Saturados* (Vol. 1, pp. 229-236). São Paulo, Brazil: Associação Brasileira de Mecânica dos Solos e Engenharia Geotécnica (in Portuguese).
- Barbosa, J.S.F., & Dominguez, J.M.L. (1996). *Mapa geológico do Estado da Bahia: texto explicativo*. Salvador: SICM (in Portuguese).
- Botelho, M.A.B., Machado, S.L., Dourado, T.C., & Amparo, N.S. (September 14-18, 2003). Experimentos laboratoriais com GPR (1GHz) em corpos arenosos para analisar a influência da água e de hidrocarbonetos na sua velocidade de propagação. In Brazilian Geophysical Society (Org.), *8th International Congress of the Brazilian Geophysical Society* (pp. 1-6). Rio de Janeiro, Brazil: Brazilian Geophysical Society (in Portuguese). https://doi.org/10.3997/2214-4609-pdb.168.arq_1021.
- Carrière, S.D., Chalikakis, K., Sénéchal, G., Danquigny, C. & Emblanch, C. (2013). Combining electrical resistivity tomography and ground penetrating radar to study geological structuring of karst unsaturated zone. *Journal of Applied Geophysics*, 94, 31-41. <http://dx.doi.org/10.1016/j.jappgeo.2013.03.014>.
- Conciani, W., Herrmann, P.S.P., Machado, S.L., & Soares, M.M. (1996). O uso da técnica de reflectometria no domínio do tempo (TDR) para determinação da umidade do solo in situ. *Solos e Rochas*, 19, 189-199 (in Portuguese).
- Cosenza, P., Marmet, E., Rejiba, F., Cui, Y.J., & Tabbagh, A. (2006). Correlations between geotechnical and electrical data: a case study at Garchy in France. *Journal of Applied Geophysics*, 60, 165-178. <http://dx.doi.org/10.1016/j.jappgeo.2006.02.003>.
- Davis, J.L., & Annan, A.P. (1989). Ground penetrating radar for high resolution mapping of soil and rock stratigraphy. *Geophysical Prospecting*, 37(5), 531-551. <http://dx.doi.org/10.1111/j.1365-2478.1989.tb02221.x>.
- Dix, C.H. (1955). Seismic velocities from surface measurements. *Geophysics*, 20, 68-86. <http://dx.doi.org/10.1190/1.1438126>.
- Evangelista, L., Silva, F., D'Onofrio, A., Di Fiore, V., Silvestri, F., Santolo, A.S., Cavuoto, G., Punzo, M., & Tarallo, D. (2017). Application of ERT and GPR geophysical testing to the subsoil characterization of cultural heritage sites in Napoli (Italy). *Measurement*, 104, 326-335. <http://dx.doi.org/10.1016/j.measurement.2016.07.042>.
- Farias, E.S. (2021). *Integração de técnicas GPR e eletrorresistividade para investigação do subsolo com foco na aplicação em geotecnia e meio ambiente* [Master's dissertation, Federal University of Bahia]. Federal University of Bahia Repository (in Portuguese). Retrieved in May 18, 2023, from http://www.geoamb.eng.ufba.br/site/sites/default/files/dissertations/erdeson_disserta_final_menor.pdf

- Ghignone, J. (1979). Geologia dos sedimentos ferozóicos do Estado da Bahia. In H.A.V. Inda (Ed.), *Geologia e recursos minerais do estado da Bahia: textos básicos* (Vol. 1, pp. 23-117). Salvador: Secretaria de Minas e Energia do Estado da Bahia (in Portuguese).
- Huber, E., & Hans, G. (June 18-21, 2018). RGPR — an open-source package to process and visualize GPR data. In Institute of Electrical and Electronics Engineers (Org.), *17th International Conference on Ground Penetrating Radar (GPR)* (pp. 1-4). New York, United States: IEEE. <https://doi.org/10.1109/ICGPR.2018.8441658>.
- Lima, O.A.L. (1999). *Caracterização hidráulica e padrões de poluição no aquífero Recôncavo na Região de Camaçari - Dias D'Avila* [Unpublished full professor thesis]. Universidade Federal da Bahia (in Portuguese).
- Machado, S.L., Botelho, M.A.B., Amparo, N.S., & Dourado, T.C. (June 26-30, 2006). The use of the Ground Penetrating Radar, GPR in environmental non intrusive diagnostic and monitoring tasks. In H.R. Thomas (Ed.), *5th ICEG Environmental Geotechnics: Opportunities, Challenges and Responsibilities for Environmental Geotechnics* (Vol. 1, pp. 549-556). London, United Kingdom: Institute of Civil Engineers.
- Machado, S.L. (2023a). Retrieved in June 14, 2023, from https://drive.google.com/file/d/1lhm60DdZfb_2m8m68In5hpS3Lu8IWPA5/view
- Machado, S.L. (2023b). Retrieved in June 14, 2023, from <https://drive.google.com/file/d/1KEX7VLRfdtnhNRwSjXKoweWBhyuwqYbz/view>
- Nguyen, S.T. (2014). Micromechanical approach for electrical resistivity and conductivity of sandstone. *Journal of Applied Geophysics*, 111, 135-140. <http://dx.doi.org/10.1016/j.jappgeo.2014.10.001>.
- Pellicer, X.M., & Gibson, P. (2011). Electrical resistivity and Ground Penetrating Radar for the characterisation of the internal architecture of Quaternary sediments in the Midlands of Ireland. *Journal of Applied Geophysics*, 75(4), 638-647. <http://dx.doi.org/10.1016/j.jappgeo.2011.09.019>.
- Sass, O., Bell, R., & Glade, T. (2008). Comparison of GPR, 2-D resistivity and traditional techniques for the subsurface exploration of the Öschingen landslide, Swabian Alb (Germany). *Geomorphology*, 93, 89-103. <http://dx.doi.org/10.1016/j.geomorph.2006.12.019>.
- Souza, J.D., Melo, R.C., & Kosin, M. (2004). Mapa geológico do Estado da Bahia. In CPRM (Org.), *Repositório Institucional de Geociências*. Retrieved in May 18, 2023, from <https://rigeo.cprm.gov.br/handle/doc/8665> (in Portuguese).
- Souza, L.A., & Gandolfo, O.C.B. (2012). Métodos geofísicos em geotecnia e geologia ambiental. *Revista Brasileira de Geologia de Engenharia e Ambiental*, 2, 9-27 (in Portuguese). Retrieved in May 18, 2023, from <https://www.abge.org.br/downloads/revistas/metodos.pdf>
- Topp, G.C., & Davis, J.L. (1981). Detecting infiltration of water through soil cracks by time-domain reflectometry. *Geoderma*, 26, 13-23. [http://dx.doi.org/10.1016/0016-7061\(81\)90073-2](http://dx.doi.org/10.1016/0016-7061(81)90073-2).
- Topp, G.C., Davis, J.L., & Annan, A.P. (1980). Electromagnetic determination of soil water content: measurements in coaxial transmission lines. *Water Resources Research*, 16(3), 574-582. <http://dx.doi.org/10.1029/WR016i003p00574>.
- Wyllie, M.R.J., Gregory, A.R., & Gardner, G.H.F. (1958). An experimental investigation of factors affecting elastic wave velocities in porous media. *Geophysics*, 23, 459-493. <http://dx.doi.org/10.1190/1.1438493>.
- Zorzi, R. R. & Rigoti, A (2011). Aplicação de métodos geoeletricos para monitoramento da barragem de concreto da UHE Gov. José Richa. *Boletim Paranaense de Geociências*, 64-65, 48-58 (in Portuguese). <http://dx.doi.org/10.5380/geo.v65i0.10481>.